PCCP

PAPER

View Article Online
View Journal | View Issue

Cite this: *Phys. Chem. Chem. Phys.*, 2023, **25**, 17609

Photochemical properties of a potential interstellar dust precursor: the electronic spectrum of $Si_3O_2^+$

Taarna Studemund, Kai Pollow, Marko Förstel and Otto Dopfer*

Silicon oxide compounds are considered as precursors for silicon-based interstellar dust grains which consist mainly of silica and silicates. Knowledge of their geometric, electronic, optical, and photochemical properties provides crucial input for astrochemical models describing the evolution of dust grains. Herein, we report the optical spectrum of mass-selected $Si_3O_2^+$ cations recorded in the 234–709 nm range by means of electronic photodissociation (EPD) in a quadrupole/time-of-flight tandem mass spectrometer coupled to a laser vaporization source. The EPD spectrum is observed predominantly in the lowest-energy fragmentation channel corresponding to Si_2O^+ (loss of SiO), while the higher-energy Si^+ channel (loss of Si_2O_2) provides only a minor contribution. The EPD spectrum exhibits two weaker unresolved bands A and B near 26 490 and 34 250 cm^{-1} (377.5 and 292 nm) and a strong transition C with a band origin at 36 914 cm^{-1} (270.9 nm) which shows vibrational fine structure. Analysis of the EPD spectrum is guided by complementary time-dependent density functional theory (TD-DFT) calculations at the UCAM-B3LYP/cc-pVTZ and UB3LYP/cc-pVTZ levels to determine structures, energies, electronic spectra, and fragmentation energies of the lowest-energy isomers. The cyclic global minimum structure with C_{2v} symmetry determined previously by infrared spectroscopy can explain the EPD spectrum well, with assignments of bands A–C to transitions from the $^2A_1$ ground electronic state (D_0) into the 4th, 9th, and 11th excited doublet states ($D_{4,9,11}$), respectively. The vibronic fine structure of band C is analyzed by Franck–Condon simulations, which confirm the isomer assignment. Significantly, the presented EPD spectrum of $Si_3O_2^+$ corresponds to the first optical spectrum of any polyatomic $Si_nO_m^+$ cation.

Received 9th June 2023,
Accepted 19th June 2023

DOI: 10.1039/d3cp02693k

rsc.li/pccp

1. Introduction

Silicon and oxygen are the most abundant elements in our Earth's crust. Both elements are major ingredients for sand, rocks, *etc.* and thus played a major role in the evolution of our planet. Not surprisingly, corresponding silicon compounds, mainly bare silica (SiO_2) and metal-containing silicates (*e.g.*, Me_2SiO_4 and $MeSiO_3$ with Me = Fe and Mg), are also observed throughout the universe, in meteorites, and in interplanetary dust grains.[1–8] In 1971, the rather stable SiO diatomic was first detected in space by radioastronomy.[9–11] However, apart from SiO, no larger polyatomic Si_nO_m molecule has yet been identified in the interstellar medium (ISM).[12] On the other hand, larger solid silicate grains have been made responsible for broad and unspecific infrared (IR) bands near 10 and 18 μm (Si–O stretch and O–Si–O bend modes) observed towards different stars and in spectra of meteorites and star dust particles.[3,4,8,13–17] They are also considered to be possible carriers of the strongest discrete interstellar extinction feature at 217.5 nm in the UV[18,19] and the broad extended red emission (ERE) in the visible to NIR range.[20,21] Linking these two size domains, from diatomic SiO towards large μm-sized dust particles in the ISM, is a long-standing challenge in astrochemistry. Several of the present theories suggest the seed formation for nucleating particles in the gas phase as well as superficial growth at the surface.[6,8,22–24] Nevertheless, details of the particle growth mechanism, the intermediates, and relevant factors such as radiation field, chemical abundance, particle and grain size distribution, and temperature remain unresolved issues for dust formation.[8,25,26] Several laboratory experiments showed that SiO can form larger aggregates even at low temperature, suggesting that bottom-up aggregation can occur without barriers.[27–29] Such Si_nO_m cluster growth has been modelled by quantum chemical methods for both stoichiometric ($n = m$) and nonstoichiometric ($n \neq m$) cases[8,19,30–32] and experimentally studied by photoionization mass spectrometry.[19,31] Further aggregation simulations included growth of metal silicates.[8,33,34] In addition to growth of

Institut für Optik und Atomare Physik, Technische Universität Berlin, Hardenbergstraße 36, 10623 Berlin, Germany. E-mail: dopfer@physik.tu-berlin.de

neutral silica and silicates, ion–molecule reactions may also significantly contribute to silicon chemistry in certain astrophysical environments due to their larger cross sections in low-density media.[35–40] To this end, the structures, energies, and ion–molecule reactions of $Si_nO_m^+$ ions have so far mostly been studied by mass spectrometry and computational chemistry.[41–51] However, exploring and understanding ionic species participating in such processes by spectroscopy in the laboratory to reveal their geometric and electronic structure and their photochemistry is a challenge, because of their high reactivity and low number density.[52]

Concerning $Si_nO_m^+$ cations, the SiO^+ dimer is rather well characterized by electronic spectroscopy and calculations.[53–58] Current knowledge about the structure, bonding, and chemical reactivity of polyatomic $Si_nO_m^+$ ions relies largely on mass spectrometry and computational chemistry.[41–47,49–51] Thus, experimental information about the geometric and electronic structure is extremely scarce. IR spectra of $(SiO)_n^+$ clusters with n = 3–5 recorded by multiple photon dissociation (IRMPD) *via* loss of SiO have been assigned to the most stable cyclic (n = 3) and bicyclic structures (n = 4–5) by comparison to DFT calculations at the B3LYP/cc-pVTZ level.[59] IRMPD spectra have also been recorded for a larger variety of Xe-tagged $Si_nO_m^+$ ions with n = 3–5 and $m = n$ and $n \pm 1$ in a broader spectral range and for colder ions.[60] The assigned lowest-energy structures reveal several recurring binding motifs, including the Si_2O_2 rhombus, the Si_3O_2 pentagon, and the Si_3O_3 hexagon. Significantly, apart from the Si-rich $Si_5O_4^+$ ion, all other assigned $Si_nO_m^+$ structures with $m \geq 4$ contain already the tetrahedral SiO_4 unit characteristic for silicates, despite their low degree of oxidation. This result may be taken as experimental evidence that interstellar silicates indeed may grow in a bottom-up approach from small silicon oxide clusters.

To investigate the electronic structure and photochemical stability of $Si_nO_m^+$ cations against radiation fields in the ISM, their optical spectra are required. However, apart from the SiO^+ dimer,[54,55,58,61] no optical spectrum of any polyatomic $Si_nO_m^+$ cation has been reported yet and, to the best of our knowledge, the same is true for polyatomic neutrals. To this end, we have initiated a few years ago a research program to systematically measure the optical spectra of mass-selected $Si_nO_m^+$ (and also $Si_nC_m^+$) cations by electronic photodissociation (EPD) in a recently constructed tandem mass spectrometer coupled to a temperature-controlled laser desorption source. This approach was initially tested and optimized by recording high-resolution vibronic spectra of gold cluster cations.[62–65] First applications of EPD spectroscopy to Si-containing cluster ions include the first spectrum of a $Si_nC_m^+$ cation (namely $Si_4C_2^+$)[66] and the first spectrum of diatomic Si_2^+.[67] Herein, we extend these efforts to $Si_3O_2^+$ and report the first optical spectrum of any polyatomic $Si_nO_m^+$ ion. The spectrum is recorded in the 234–709 nm range and its interpretation is guided by complementary time-dependent density functional theory (TD-DFT) calculations using various functionals. The $Si_3O_2^+$ ion has been chosen as a promising target for several reasons. First, its structure in the ground electronic state has already been determined as a planar cyclic pentagon with C_{2v} symmetry from our previously reported IR spectrum, yielding several vibrational frequencies in its $^2A_1$ ground state.[60] This structure is indeed computed to be the lowest energy isomer.[42,60] Second, our initial experiments have indicated high abundance of this ion by reacting O_2 with a plasma generated by laser vaporization of a Si rod. Third, the generated $Si_3O_2^+$ ions show strong absorption and resulting fragmentation at 355 nm. Further previous work on $Si_3O_2^+$ includes mass spectrometry, demonstrating its generation from laser vaporization of SiO targets at various wavelengths.[42,43] In addition, the dissociation into Si_2O^+ and SiO was predicted to be the lowest-energy fragment channel.[42] The analysis of the kinetic energy release upon metastable decay of $Si_3O_2^+$ into SiO using the Klots evaporation ensemble and Rice-Ramsperger-Kassel (RRK) models yielded dissociation energies of 0.75 and 1.06 eV, respectively,[44] much lower than those calculated for a variety of $Si_nO_m^+$ ions including $Si_3O_2^+$ (2–4 eV).[42]

2. Experimental setup and computational methods

EPD spectra of $Si_3O_2^+$ are recorded in the range of 1.75–5.30 eV (14 104–42 735 cm^{-1}, 234–709 nm) using a quadrupole/time-of-flight tandem mass spectrometer described in detail elsewhere.[68,69] Briefly, $Si_nO_m^+$ clusters are generated in a pulsed laser vaporization source by focusing a Q-switched Nd:YAG laser pulse (532 nm, 2–10 mJ, 20 Hz, diameter 0.5 mm) onto a rotating and translating Si rod (American Elements, 99.9%) using a lens with f = 28 cm. The generated silicon plasma is seeded in a pulsed carrier gas mixture (6–10 bar) composed of O_2/He (1 : 4000) or O_2/Ar (1 : 1000–1 : 2000). $Si_nO_m^+$ clusters are formed in a reaction channel and expanded into vacuum through a temperature-controlled nozzle cooled to 90–150 K. After passing through a skimmer, the desired $Si_3O_2^+$ clusters (m/z 116) are filtered by a quadrupole mass spectrometer and guided through an Einzel lens system into the extraction region of an orthogonal reflectron time-of-flight mass spectrometer (ReTOF-MS). Here, $Si_3O_2^+$ clusters are irradiated with a laser pulse (2–4 mJ) emitted from a commercial, tunable optical parametric oscillator (OPO, 5–10 cm^{-1} bandwidth, 192–2750 nm tuning range, 0.5–150 mJ per pulse, 10 Hz) pumped by a Q-switched Nd:YAG laser (355 nm, 290 mJ) to induce resonant photodissociation. Parent and fragment ions are detected at the end of the ReTOF-MS using a microchannel plate detector. While the vaporization laser operates at 20 Hz, the OPO dissociation laser runs at 10 Hz (laser-on signal). The laser-induced dissociation signal is measured shot-by-shot and allows the normalization of the photodissociation yield by the parent signal using the laser-on signals and the photon flux. The yield of the remaining parent ions as well as the observed fragment ions (Si_2O^+ and Si^+) are monitored as a function of the photon energy to determine the total EPD cross section using a modified Beer–Lambert law described in detail previously.[69–71] For each wavelength, 200–300 mass spectra are averaged. For the analysis, we only consider the monoisotopic species. Initially, the whole spectral range (234–709 nm) is scanned in 1 nm steps to obtain an overview spectrum. The interesting ranges exhibiting resonant absorption

bands are then measured at a reduced step size of 0.02–0.2 nm depending on the range (0.02 nm for 254.4–272 nm, 0.05 nm for 292–399 nm, 0.1 nm for 656–709.4 nm, 0.2 nm for 400–657 nm). The obtained EPD spectra provide a reasonable approximation to the total absorption cross section when neglecting competing (nonradiative and radiative) relaxation channels and assuming a single-photon absorption process. The uncertainty of the determined EPD cross section depends on the error of the overlap factor ($\alpha = 0.6 \pm 0.3$) between the molecular ion beam and the laser beam, which depends somewhat on the spectral range.

DFT calculations coupled with a basin-hopping algorithm are performed to find the lowest-energy isomers of $Si_3O_2^+$.[72] Using the previously described algorithm at the RI-BP86/def-SVP level of theory[73,74] as implemented in the TURBOMOLE V6.3 program package,[75] we identify eight nonequivalent minima. The already known cyclic structure determined by IR spectroscopy and previous calculations is the most stable isomer.[44,60,76] The eight lowest-energy nonequivalent structures are further optimized at the higher UCAM-B3LYP/cc-pVTZ level including the Grimme dispersion correction with Becke–Johnson damping (GD3BJ)[77,78] using the GAUSSIAN16 program package.[79] For comparison, additional calculations are performed at the UB3LYP/cc-pVTZ level, which yield results similar to the UCAM-B3LYP data. Moreover, Lu *et al.* found similar energies for Si_nO_m clusters calculated at the MP2 and B3LYP level.[80] In addition to the doublet electronic states, quartet states for the four lowest lying isomers are investigated and found to be much higher in energy (by 2.359, 2.595, 3.515, 1.656 eV for isomers **I–IV**), similar to the results of previous studies for anions.[76,81] Hence, they are not considered further. Calculations for neutral Si_3O_2 are also performed and reveal good agreement with earlier results.[19,60,76,81] Harmonic vibrational frequencies are determined for all stationary points to verify their nature as minima or transition states. They are also used to derive relative energies (E_0) and dissociation energies (D_0) corrected for vibrational zero-point energy. Optical spectra are computed by vertical TD-DFT calculations at the UCAM-B3LYP/cc-pVTZ and UB3LYP/cc-pVTZ levels, which yield excitation energies and oscillator strengths of the first 100 vertical transitions for each isomer. To assign resolved vibrational structure, Franck–Condon (FC) simulations including Herzberg–Teller coupling are employed as implemented in GAUSSIAN16. The charge distribution is analyzed by natural bond orbital (NBO) analysis, while natural transition orbitals (NTO) are employed for visualizing the orbitals involved in the respective excitations.

3. Results and discussion

3.1 Computational results

The four most stable $Si_3O_2^+$ isomers (**I–IV**) found are shown in Fig. 1, along with their salient structural parameters, relative energies, and symmetries of the electronic ground state obtained at the UCAM-B3LYP level. The cyclic global minimum **I** ($^2A_1$, C_{2v}) has a planar five-membered monocyclic ring with a rather long Si–Si bond (2.901 Å), in good agreement with

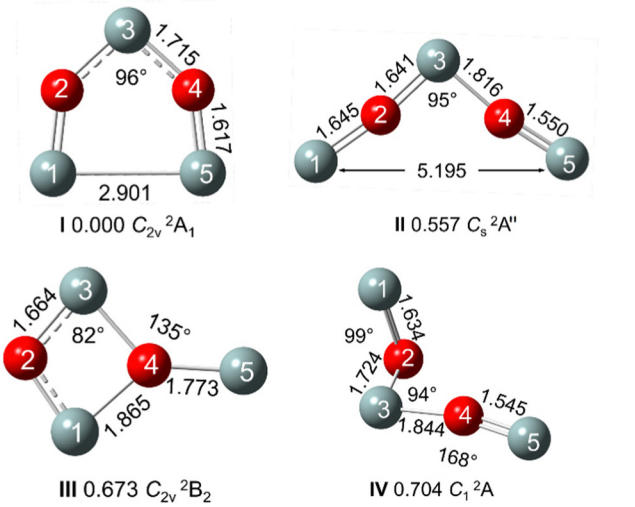

Fig. 1 Minimum structures of the four lowest lying $Si_3O_2^+$ isomers (**I–IV**) calculated at the UCAM-B3LYP/cc-pVTZ level, along with bond lengths [Å], selected bond angles [°], relative energy (E_0 in eV), and structural and electronic symmetries.

previous computations.[42,60] Isomer **II** ($^2A''$, C_s) lies E_0 = 0.557 eV higher in energy and results formally from isomer **I** by breaking this Si–Si bond. This leads to an asymmetric structure with different Si–O bond lengths in both arms of the V-shaped structure, *i.e.* the loss of the C_2 rotational symmetry. In fact, ring opening of the ground state (D_0) of isomer **I** produces the first excited state of isomer **II** (D_1), while ring closure of the ground state of isomer **II** (D_0) converges to the first excited state (D_1) of isomer **I** (when keeping the electronic configuration and neglecting any conical intersections). This view is not only confirmed by potential energy scans along the ring opening angle but also by the symmetry of the electronic configurations (reducing the C_{2v} symmetry of **I** to C_s transforms the D_0 state from $^2A_1$ into $^2A'$, while the D_0 state of **II** has a $^2A''$ configuration). As a result, there is no transition state for interconversion of isomers **I** and **II** on their ground state potentials. In this sense, isomer **II** should formally be considered an excited state of isomer **I**. Nonetheless, we consider isomer **II** for the analysis of the EPD spectrum because it may be formed and kinetically trapped as metastable species in the ion source because of long lifetime resulting from the large geometry change to the minimum **I**. The planar isomer **III** (0.673 eV, $^2B_2$, C_{2v}) has a four-membered Si_2O_2 rhombic ring with a dangling O–Si bond, while isomer **IV** (0.704 eV, ^2A, C_1) has a chain-like structure without any symmetry. In all four structures in Fig. 1, each O atom binds to two Si atoms, except for isomer **III** in which one O atom binds to three Si atoms. The computations at the UB3LYP level yield similar results, with the major difference that isomer **II** has a C_{2v} symmetric structure with a $^2B_1$ electronic state and the change in energetic ordering of the nearly isoenergetic isomers **III** and **IV** (E_0 = 0, 0.343, 0.778, 0.671 eV for **I–IV**). In all four isomers, there is no bond between the two O atoms, which in turn bind mostly to two Si atoms according to its divalent character. Only, in **III** one of the

O atoms binds to three Si atoms. As isomers **V–VIII** have relative energies (1.40, 3.19, 4.23, and 4.46 eV) significantly higher than 1 eV, we do not consider them further. Indeed, according to our previous experience with spectroscopy of $Si_nX_m^{(+)}$ clusters (X = C, B, O), such laser vaporization sources predominantly produce the global minimum structure.[66,68,82,83]

The calculated dissociation energies (D_0) for the various fragmentation channels of $Si_3O_2^+$ obtained for both computational levels are listed in Table 1. They are given with respect to isomer **I** and are quite similar for both considered DFT levels. Only dissociation into two fragments is considered because three-body fragmentation is usually more energy demanding due to the rupture of more chemical bonds. The lowest dissociation channel is $Si_2O^+ + SiO$ (D_0 = 2.60 eV), because of the strong chemical bond of neutral SiO (D_0 = 8.26 ± 0.06 eV).[84] Potential energy surface scans indicate that this dissociation occurs without a reverse reaction barrier (*i.e.* the appearance energy is equal to D_0). It is followed by $Si^+ + Si_2O_2$ (D_0 = 3.56 eV) because of the low ionization energy of Si (8.15 eV).[85] The third channel is $Si + Si_2O_2^+$ (D_0 = 4.70 eV). All other channels require more than 6 eV and are thus far beyond the investigated spectral range (<5.3 eV). Overall, the dissociation energies obtained at the UB3LYP level are close to those at the UCAM-B3LYP level (Table 1), with deviations of ≤ 0.32 eV for the channels below 9 eV. Significantly, our computed binding energy for SiO loss is much higher and probably more reliable than those values inferred in a rather indirect analysis of experimental kinetic energy release data (D_0 = 0.75 and 1.06 eV).[44]

In Table 2, we summarize the vertical excitation energies of the D_n excited states (up to n = 16) for isomer **I** obtained at the UCAM-B3LYP level, along with their oscillator strengths (f). Excitation energies range from 0.9 to 5.6 eV, and the transitions into the D_4, D_9, D_{11}, and D_{15} states at 3.55, 3.95, 4.7, and 5.55 eV have by far the highest oscillator strengths (f = 0.03–0.4), while f < 0.005 for all other excitations. The spectrum predicted for isomer **II** is very different, with the most intense transitions with significant oscillator strength being into the D_2, D_4, D_{11}, D_{12}, D_{15}, and D_{16} states at 0.92, 1.86, 4.19, 4.46, 5.07 and 5.26 eV (f = 0.09, 0.05, 0.02, 0.03, 0.02, and 0.02). The excitation spectra of **III** and **IV** will be briefly considered below.

Table 1 Dissociation energies (D_0 in eV) of the most stable isomer **I** of $Si_3O_2^+$ into all possible two-body fragment channels calculated at the UCAM-B3LYP and UB3LYP levels (cc-pVTZ basis set)[a]

Fragments	UCAM-B3LYP	UB3LYP
$Si_2O^+ + SiO$ ($^2\Pi_g + {}^1\Sigma^+$)	**2.60**	**2.48**
$Si^+ + Si_2O_2$ ($^2P_{1/2} + {}^1A_g$)	**3.55**	**3.74**
$Si_2O_2^+ + Si$ ($^2B_{1u} + {}^3P_0$)	4.70	4.71
$Si_2^+ + SiO_2$ ($^4\Sigma_g^- + {}^1A_1$)	6.42	6.18
$SiO^+ + Si_2O$ ($^2\Sigma^+ + {}^3\Sigma_g$)	7.06	6.90
$Si_3O^+ + O$ ($^2B_{1u} + {}^3P_2$)	8.09	7.77
$Si_3^+ + O_2$ ($^2B_2 + {}^3\Sigma_g^-$)	9.75	9.53
$SiO_2^+ + Si_2$ ($^2A_2 + {}^3\Sigma_g^-$)	10.98	10.55
$O_2^+ + Si_3$ ($^2\Pi_g + {}^3B_2$)	14.22	13.82
$O^+ + Si_3O$ ($^4S_{3/2} + {}^3A''$)	14.70	14.48

[a] Observed fragment channels are indicated in bold. For each fragment, the most stable structure with lowest-energy spin multiplicity is used.

Table 2 Multiplicity, symmetry, vertical excitation energy (E_v), and oscillator strength (f) of the excited states (D_n) of isomer **I** of $Si_3O_2^+$ calculated at the UCAM-B3LYP/cc-pVTZ level[a]

State	E_v/eV (cm^{-1})	f	State	E_v/eV (cm^{-1})	f
$D_0(^2A_1)$	0		**$D_9(^2B_1)$**	**3.953 (31 885)**	**0.0276**
$D_1(^2B_1)$	0.936 (7552)	0.0006	$D_{10}(^2A_1)$	4.569 (36 849)	0.0062
$D_2(^2A_2)$	2.290 (18 473)	0.0000	**$D_{11}(^2B_2)$**	**4.702 (37 923)**	**0.3925**
$D_3(^2B_1)$	2.462 (19 855)	0.0000	$D_{12}(^2B_1)$	4.918 (39 665)	0.0002
$D_4(^2B_2)$	**3.553 (28 652)**	**0.0334**	$D_{13}(^2A_2)$	5.213 (42 049)	0.0000
$D_5(^2A_2)$	3.688 (29 749)	0.0000	$D_{14}(^2A_2)$	5.548 (44 745)	0.0000
$D_6(^2B_1)$	3.727 (30 059)	0.0042	$D_{15}(^2B_2)$	5.548 (44 749)	0.0309
$D_7(^2A_1)$	3.833 (30 917)	0.0029	$D_{16}(^2A_2)$	5.619 (45 317)	0.0000
$D_8(^2B_1)$	3.891 (31 380)	0.0037			

[a] The D_4, D_9, and D_{11} states assigned to bands A–C in the EPD spectrum are indicated in bold.

3.2 Experimental results

The typical mass spectrum of the laser vaporization ion source in Fig. 2 shows a broad distribution of $Si_nO_m^+$ clusters in the range m/z 30–345. The relative intensities and overall shape of the mass spectrum can strongly be modified by several parameters of the ion source, such as energy, focus, and timing of the desorption laser, composition and pressure of carrier gas, and extraction time of the high voltage pulses of the ReTOF. The spectrum in Fig. 2 shows high yields for O-poor $Si_nO_m^+$ clusters with m = 0–2. Due to the low concentration of O_2 in the carrier gas, pure Si_n^+ clusters are rather abundant. The conditions are optimized for the production of $Si_3O_2^+$ (m/z 116), which is indeed the ion with highest abundance. Other prominent peaks correspond to m/z 72 (Si_2O^+), 88 ($Si_2O_2^+$), 168 (Si_6^+), 196 (Si_7^+), 224 (Si_8^+), 240 (Si_8O^+), 252 (Si_9^+), 270 (Si_9O^+), 280 (Si_{10}^+), 296 ($Si_{10}O^+$), and 308 (Si_{11}^+). The assignment of these mass peaks is fully confirmed by their isotope pattern arising from the natural isotope abundance of Si (92.2, 4.7, 3.1% for $^{28/29/30}$Si). Initial EPD experiments of several abundant $Si_nO_m^+$ ions at 355 nm have shown substantial fragmentation of $Si_3O_2^+$, which has thus been selected as our first target for both TD-DFT calculations and wavelength-dependent EPD spectra.

The obtained ReTOF mass spectrum after selecting $Si_3O_2^+$ with the quadrupole (laser off) is compared in Fig. 3 to the

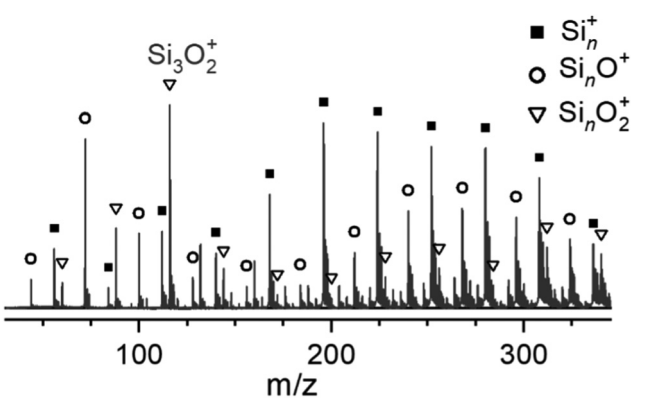

Fig. 2 Mass spectrum of $Si_nO_m^+$ ions produced by using laser vaporization of a pure Si rod and an expansion of O_2/He.

summed mass spectrum resulting from scanning the OPO laser from 264 to 272 nm (laser on). In these experiments, the quadrupole is set to transmit all isotopologues of $Si_3O_2^+$. Their relative intensities confirm the identification of the *m/z* 116 ion as essentially pure $Si_3O_2^+$. The additional photofragment ion signal present in the laser-on spectrum at *m/z* 72–74 is assigned to Si_2O^+ and arises from loss of SiO. The fragmentation yield is in the order of 30% for the strongest absorption at 4.58 eV (270.9 nm, band C0), which demonstrates good overlap between laser and ion beams. The second and rather minor fragment channel at *m/z* 28–30 corresponds to Si^+ and arises from loss of neutral Si_2O_2. Although this channel is roughly two orders of magnitude weaker, we consider both for generating the total EPD spectrum. These two observed fragment channels are also the lowest dissociation channels predicted by the DFT calculations, with D_0 = 2.60 and 3.55 eV (476.9 and 349.3 nm, 20 970 and 28 632 cm^{-1}). Both lowest-energy fragmentation channels are readily accessible by single-photon absorption in the spectral range employed for these mass spectra. The photofragmentation branching ratio of roughly 10^2/1 into Si_2O^+/Si^+ is consistent with density of state arguments strongly favoring the lower energy channel. The third-lowest channel producing $Si_2O_2^+$ and Si is predicted to require 4.70 eV (263.8 nm, 37 910 cm^{-1}), which is close to the highest employed photon energies and thus not detected. The absence of this and other higher-energy channels indicate single-photon absorption conditions. We can also exclude the scenario that the Si_2O_2 loss channel arises from sequential loss of two SiO molecules, because (i) this three-body channel would be much higher in energy and (ii) according to our preliminary data the potential intermediate Si_2O^+ cation does not absorb at the same energies as $Si_3O_2^+$.

The total EPD cross section measured for $Si_3O_2^+$ is compared in Fig. 4 to vertical absorption spectra computed for isomers **I–IV** at the UCAM-B3LYP level. Computed stick spectra are convoluted with a Gaussian line profile (FWHM of 0.23 eV) for more convenient comparison with the EPD spectrum. The EPD spectrum in Fig. 4 is composed of several shorter scans, taken at different step sizes and various nozzle temperatures (90–120 K) as described in Section 2. Furthermore, the range 400–709 nm is only measured using the O_2/He mixture (dashed trace in Fig. 4), because no EPD signal is observed. This observation is consistent with the computed dissociation energy of 476.9 nm (D_0 = 2.60 eV, 20 970 cm^{-1}) and the absence of any significant predicted absorption of isomer **I** below 3.5 eV (<28 000 cm^{-1}, > 360 nm). The spectrum below 400 nm is investigated with both the O_2/Ar and the O_2/He mixture. However, the spectra measured with the O_2/Ar mixture are better resolved due to colder $Si_3O_2^+$ ions and thus used for evaluating the EPD spectrum below 400 nm.

The EPD spectrum of $Si_3O_2^+$ exhibits three bands A–C with peak maxima at 26 490, 34 250, and 36 914 cm^{-1} (377.5, 292.0, and 270.9 nm; 3.284, 4.246, and 4.577 eV). While the broad and unresolved bands A and B (with widths of FWHM = 760 and 285 cm^{-1}) are rather weak, the intense band C shows vibrational fine structure. The measured EPD spectrum shows good agreement with the vertical spectrum predicted for isomer **I**

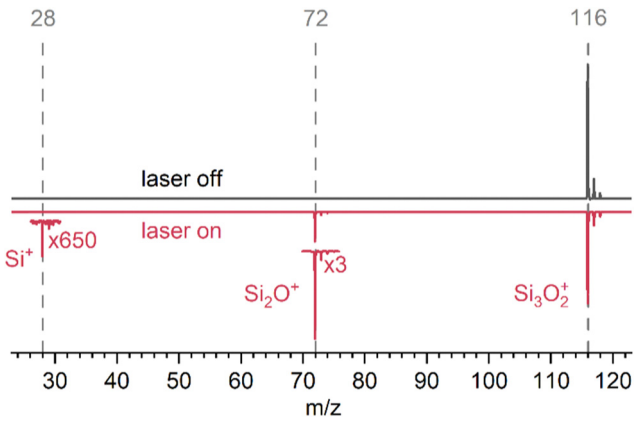

Fig. 3 Mass spectrum of $Si_3O_2^+$ (*m/z* 116, O_2/Ar carrier gas, *T* = 90 K) mass-selected with the quadrupole with transmission of all isotopologues for OPO laser off (black) and on (red) measured with the ReTOF-MS. The laser-on spectrum is summed over all mass spectra obtained for λ = 264–272 nm. The range of the observed fragments Si^+ (*m/z* 28) and Si_2O^+ (*m/z* 72) are vertically expanded by factors of 650 and 3, respectively. To generate the EPD spectrum, the signals from the laser-on spectra of the monoisotopic species are used.

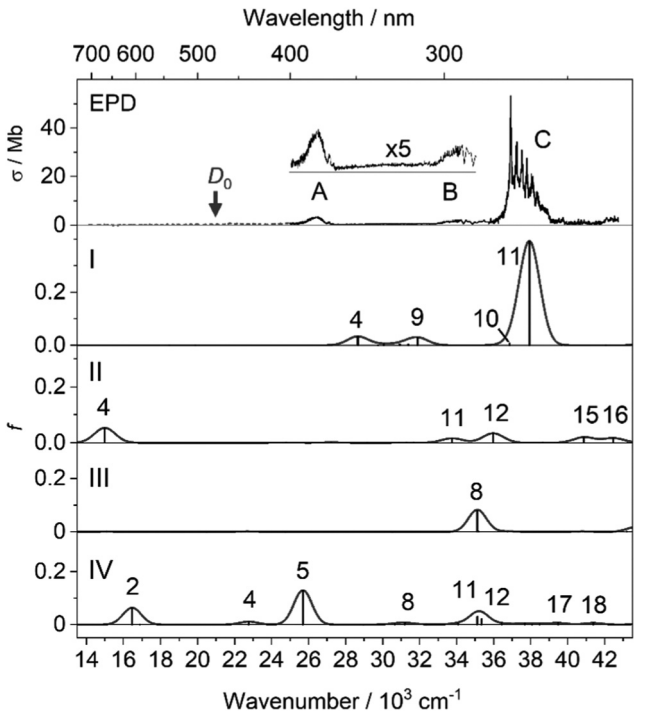

Fig. 4 Total EPD spectrum of $Si_3O_2^+$ recorded in the Si_2O^+ and Si^+ fragment channels (cross section σ) compared to vertical absorption spectra (oscillator strength *f*) of the four lowest lying isomers **I–IV** calculated at the UCAM-B3LYP/cc-pVTZ level (Table 2). The dashed line in the EPD spectrum represents the range scanned using the O_2/He mixture, while scans measured with the O_2/Ar gas mixture are shown with a solid line. Part of the EPD spectrum is also vertically expanded by a factor of 5 to show the weak features A and B. Excited states with $f \geq 0.005$ are labeled. The calculated dissociation energy D_0 = 2.60 eV (20 970 cm^{-1}) is indicated by an arrow.

with respect to band positions and relative intensities, while the spectrum of isomer **II** does not match when assuming it to be the single carrier of the EPD spectrum. Specifically, bands A–C are assigned to the three strongly allowed and thus intense $D_4 \leftarrow D_0$ ($^2B_2 \leftarrow {}^2A_1$), $D_9 \leftarrow D_0$ ($^2B_1 \leftarrow {}^2A_1$), and $D_{11} \leftarrow D_0$ ($^2B_2 \leftarrow {}^2A_2$) transitions of **I** predicted at 3.553, 3.953, and 4.702 eV, with deviations of 0.269, −0.293, and 0.125 eV from the observed band maxima, which are well within the accepted error of ±0.3 eV for TD-DFT calculations for excited state energies. Although some bands of isomers **II**, **III** and **IV** are close to the bands observed in the EPD spectrum, we exclude them as important carriers of the experimental spectrum, because (i) of their higher relative energy, (ii) the type of employed laser desorption source produces usually the most stable isomer of (doped) silicon clusters, and (iii) isomer **I** was clearly identified as single carrier of the IR spectrum measured for Xe-tagged $Si_3O_2^+$.[60] All bands A–C are observed in the Si_2O^+ channel, and this result is consistent with single-photon absorption from the ground state, because all excited states lie at least 0.6 eV above the energy for barrierless dissociation into this channel (D_0 = 2.60 eV). On the other hand, only bands B and C are observed with noticeable intensity in the much weaker Si^+ fragment channel (with a spectrum similar to that detected in the Si_2O^+ channel). Indeed, band A at 3.28 eV (D_4 state) occurs below its predicted dissociation energy of (D_0 = 3.55 eV) and thus the predicted fragment appearance energies are also consistent with the experimental detection of isomer **I**.

Bands A and B do not show any resolved vibronic structure, which may arise from large geometry changes giving rise to FC congestion and/or short lifetimes of the excited states arising from fast nonradiative decay (such as internal conversion to lower electronic states or dissociation). In contrast, the higher energy band C is vibrationally resolved and appears at first glance as a simple progression of peaks C0–C5, spaced by roughly 300 cm^{-1} (317, 293, 261, 291, and 274 cm^{-1}) to the blue of the band origin at 36 914 cm^{-1} (4.577 eV, 270.90 nm). The nonmonotonic change in the spacing provides a first indication that the progression is in fact not due to a single vibrational progression but arises from excitation of multiple modes. To assign the vibrational structure, we employ FC simulations for the $D_{11} \leftarrow D_0$ transition of isomer **I**. To this end, the D_{11} state is optimized at the UCAM-B3LYP level and the geometry changes upon electronic excitation are listed in Table 3, while vibrational normal modes are shown in Fig. 6 with frequencies listed in Table 3. All bond lengths slightly increase upon D_{11} excitation, while the bond angles remain nearly unchanged. The adiabatic transition energy of E_a = 37 698 cm^{-1} (4.674 eV) is only 0.028 eV lower than the vertical excitation energy of 4.702 eV (37 923 cm^{-1}), consistent with the rather small geometry change. This result is in line with the band origin C0 being the most intense vibronic band in the $D_{11} \leftarrow D_0$ transition. Moreover, the computed adiabatic transition energy agrees well with the measured band origin, with a deviation of only 922 cm^{-1} (0.114 eV). The $D_{11} \leftarrow D_0$ transition is a multicomponent excitation, mainly composed of 33α ← 29α (33%) and 29β ← 27β (54%). As 29α is the SOMO (a_1) of the cation, these excitations correspond to (LUMO+3)α ← (SOMO)α and (SOMO)β ← (SOMO-2)β. NBO analysis of the bonding and antibonding character of these orbitals indicates that the overall net effects nearly cancel for all bonds, which explains the minor geometry change upon electronic D_{11} excitation also from an orbital analysis.

Table 3 Adiabatic energies (eV), geometric parameters (Å, degrees) and vibrational frequencies (cm^{-1}) of the D_0 ground and D_{11} excited states of isomer **I** of $Si_3O_2^+$ calculated at the UCAM-B3LYP/cc-pVTZ level[a]

	$D_0(^2A_1)$	$D_{11}(^2B_2)$
E_0	0.000	4.674 (37 906)
r_{12}	1.617	1.625 (+0.008)
r_{23}	1.715	1.725 (+0.010)
r_{15}	2.901	2.963 (+0.062)
θ_{123}	138.6	139.1 (+0.5)
θ_{234}	95.5	95.9 (+0.4)
θ_{451}	83.6	82.9 (−0.7)
$\nu_1(a_1)$	1046 (*1002*)	975 (−7%)
$\nu_2(a_1)$	618 (*626*)	580 (−9%)
$\nu_3(a_1)$	406 (*398*)	384 (+5%)
$\nu_4(a_1)$	196	338 (+72%)
$\nu_5(a_2)$	147	162 (+10%)
$\nu_6(b_1)$	172	96 (−44%)
$\nu_7(b_2)$	863	1005 (+16%)
$\nu_8(b_2)$	575 (*582*)	592 (+3.0%)
$\nu_9(b_2)$	228	395 (+73%)

[a] Experimental frequencies of $Si_3O_2^+$-Xe in the D_0 state are listed in italics (in parentheses).[60]

The nine normal modes of isomer **I** can be classified as $4a_1 + a_2 + b_1 + 3b_2$. Seven of them are in-plane modes ($\nu_{1-4,7-9}$), while the two lowest-frequency modes are out-of-plane ($\nu_{5,6}$). The normal coordinates (*i.e.*, the direction and amplitudes of the elongations) are not much affected upon D_{11} excitation, although some of their frequencies change drastically (Table 3), implying that the Duschinsky matrix is nearly diagonal. For example, the Si–Si stretch frequency ν_4 increases by 72% from 196 to 338 cm^{-1}, while the other stretch modes ($\nu_{1-3,7}$) remain less affected ($\leq$16%), in line with the small change in bond lengths. Other strongly affected modes are the in-plane bend ν_9 (+73%) and the out-of-plane bend ν_6 (−44%), indicating that the out-of-plane force field changes drastically upon electronic excitation.

The initial FC simulation is performed at T = 1 K to avoid any contribution of hot bands and to analyze the vibrational structure of the D_{11} state (Fig. 5). For convenient comparison, the stick spectrum is convoluted with a Gaussian line profile with a FWHM of 80 cm^{-1} (0.01 eV), corresponding roughly to the FWHM of the measured peaks (Table 4). Moreover, the computed spectrum is shifted by −922 cm^{-1} (−0.113 eV) to the red to match the calculated and observed band origins. The employed OPO laser has a bandwidth of 10 cm^{-1} so that the broadening of the C0 (and the other) bands is not a result of the limited laser resolution but must arise from lifetime broadening and/or incompletely resolved vibrational structure, mostly arising from sequence hot bands. Part of the broadening may also come from a short excited-state lifetime with respect to fast dissociation or internal conversion processes. In contrast to the first-glance interpretation of a single vibrational progression of a mode with 300 cm^{-1}, the FC simulation reveals the activity of several modes

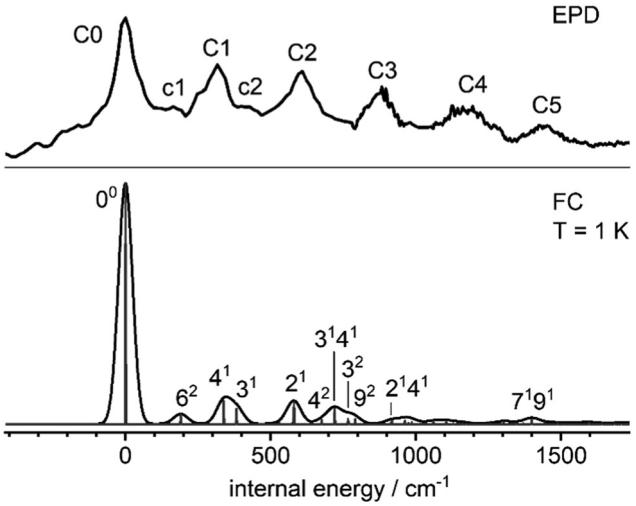

Fig. 5 Band C of the experimental EPD spectrum of $Si_3O_2^+$ compared to harmonic Franck–Condon simulation for T = 1 K (*i.e.*, without hot bands) as a function of internal energy, along with vibrational assignments (Table 4). The band origin (0^0) of the computed spectrum is redshifted by 992 cm^{-1} to match the measured one at C0 = 36 914 cm^{-1}.

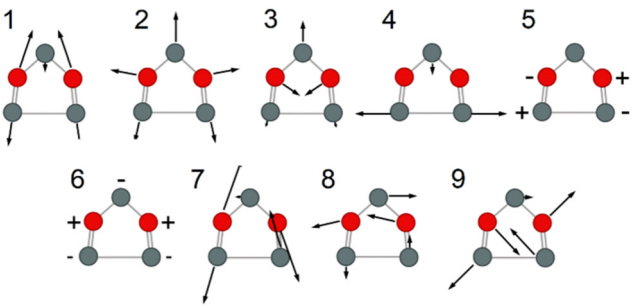

Fig. 6 Normal modes (ν_{1-9}) of isomer **I** of $Si_3O_2^+$ in the D_0 state (Table 3) computed at the UCAM-B3LYP level. The corresponding normal modes of the D_{11} state are quite similar.

as indicated in Fig. 5. According to the FC principle, only totally symmetric a_1 vibrations can be excited from the vibrationless D_0 ground state. These include progressions of a_1 modes as well as overtones and combination bands of a_1 symmetry. Indeed, the FC spectrum is dominated by progressions and combinations of all three low-frequency a_1 stretching modes ν_{2-4}, in line with the slight elongation of all bonds upon D_{11} excitation. Small contributions are provided by overtones of the out-of-plane and in-plane bends ν_6 and ν_9, along with the combination $\nu_7 + \nu_9$. Overall, the FC simulation agrees well with the measured EPD spectrum with respect to both band positions and relative intensities, confirming the assignment of both the isomer and the electronic state. A detailed assignment of the major bands C0–C5 as well as the minor features c1–c2 is listed in Table 4.

Additional FC simulations at variable elevated temperatures are performed to estimate the vibrational temperature of the ions. To this end, we focus particularly on the lower frequency side of the 0^0 origin because the appearance of the spectrum in this range is less affected by discrepancies between computed

Table 4 Experimental frequencies and widths (FWHM in parentheses) compared to computed frequencies (cm^{-1}) of the Franck–Condon simulation (Fig. 5), along with vibrational assignments and relative intensities (I)

Band	Exp [a]	Calc[a]	Assignment	I^b
C0	0 (63)	0	0^0	1.000
c1	164	192	6^2	0.041
C1	316 (85)	338	4^1	0.096
c2	400	384	3^1	0.060
C2	609 (85)	580	2^1	0.093
		677	4^2	0.017
		721	3^14^1	0.064
		767	3^2	0.021
C3	882 (97)	790	9^2	0.021
		919	2^14^1	0.014
		964	2^13^1	0.014
		987	8^19^1	0.008
C4	1196 (115)	1060	3^14^2	0.012
		1105	3^24^1	0.011
C5	1438 (99)	1302	$2^13^14^1$	0.009
		1400	7^19^1	0.020

[a] Relative frequencies with respect to the 0^0 transition at 36 914 cm^{-1}. [b] Only transitions with $I > 0.001$ are listed.

and experimental frequencies. As expected, the hot band contributions are dominated by the population of levels of the lowest-frequency out-of-plane modes ν_5 and ν_6 computed as 147 and 172 cm^{-1}. Indeed, the population of their levels can largely reproduce the shape and relative intensity of the EPD spectrum in the red wing of the 0^0 origin for vibrational temperatures of the order of T = 500 ± 200 K, indicating incomplete cooling of the ions in the cryogenic nozzle. Both collisional cooling and heating by the condensation energy released by the formation of the strong Si–O bonds affect the temperature. Similar nonequilibrium effects have been observed in EPD spectra recorded for Si_2^+ in the same setup.[67]

It is instructive to compare the properties of $Si_3O_2^+$ with those of its potential neutral precursor because photoionization could be one of the production routes in the ISM. Most calculations[76,86] including ours predict that neutral Si_3O_2 has a planar cyclic structure (C_{2v}) similar to that of isomer **I** of the cation (Fig. 1), with a $^3B_1$ ground state arising from the orbital configuration ... $(a_1)^1(b_1)^1$ and following structural parameters: r_{12} = 1.676 Å, r_{23} = 1.676 Å, r_{15} = 2.446 Å, θ_{123} = 128.8°, θ_{234} = 99.0°, and θ_{451} = 91.8°. Ionization into the $^2A_1$ cation ground state of $Si_3O_2^+$ occurs by removing an electron from the b_1 HOMO and requires an adiabatic ionization energy of 6.847 eV (181.1 nm). As the b_1 orbital is a bonding orbital of the Si–Si bond, the major structural change upon ionization is a drastic elongation of the Si–Si bond by 0.455 Å (or 19%) from r_{12} = 2.446 to 2.901 Å (corresponding to a change in formal bond order from 1 to 0.5). This view is further confirmed by the NBO charge analysis, predicting nearly all positive excess charge on these two Si atoms of the Si–Si bond (0.994 e), in agreement with previous calculations.[42] Alternative routes for the production of $Si_3O_2^+$ in the ISM include ion–molecule aggregation reactions (*e.g.*, $Si^+ + Si_2O_2$, $Si^+ + 2SiO$, $Si_2O^+ + SiO$), which appear to occur without barrier and are reverse reactions of the considered photodissociation processes (*i.e.*, photoassociation), or bimolecular ion–molecule reactions. As no optical spectra have yet

been reported for any Si_nO_m molecule, information on their electronic structure relies mainly on photoelectron spectroscopy of corresponding anion clusters[81,87,88] and rough quantum chemical calculations of HOMO–LUMO gaps.[76,80] Although these studies suggest that neutral Si_nO_m clusters may also absorb in the visible to ultraviolet range, no details have been reported yet. Our vertical TD-DFT calculations indicate that pentagonal Si_3O_2 has indeed significant absorptions in spectral ranges similar to those of the cation. For example, the strongest transitions below 5.40 eV from the $^3B_1$ ground state are predicted into the 4th, 6th, and 14th excited triplet states at 3.16, 3.35, and 5.20 eV (f = 0.026, 0.1233, and 0.1349).

4. Conclusions

The optical spectrum of mass-selected $Si_3O_2^+$ ions is measured *via* photodissociation and analyzed with complementary TD-DFT calculations. The EPD spectrum measured in the 1.75–5.30 eV range exhibits three electronic transitions A–C centered at 3.284, 4.246, and 4.577 eV and assigned to the strongest optically allowed transitions predicted for the most stable cyclic ring isomer **I** ($D_{4,9,11}$). In line with computed dissociation energies for two-body fragmentation, the main fragmentation channel is loss of SiO (D_0 = 2.60 eV), whereas the more energy-demanding loss of Si_2O_2 is two orders of magnitude weaker. While the weak bands A and B are broad and unresolved, band C shows resolved vibronic fine structure, which can well be reproduced by FC simulations of the $D_{11} \leftarrow D_0$ transition of isomer **I**, thus strongly supporting the given structural and electronic assignment.

Significantly, the presented EPD spectrum of $Si_3O_2^+$ provides the first experimental information about the electronic structure and photochemistry of any polyatomic $Si_nO_m^+$ cation. This combined strategy is generally applicable to other $Si_nO_m^+$ ions and thus paves the way for improving our understanding for the bottom-up growth (and photodestruction) mechanisms of interstellar silicate dust particles *via* a cation reaction route at the molecular level. To this end, similar studies are currently underway for other small $Si_nO_m^+$ cations. These studies may eventually enable to identify such species in the ISM, which then can contribute to the development of strongly-needed realistic models for the bottom-up growth of silicates in such environments. In addition, these experimental spectra serve as valuable benchmark for developing and testing computational approaches for (highly) excited electronic states of such clusters, which provides still a challenge to computational chemistry.

Conflicts of interest

There are no conflicts to declare.

Acknowledgements

This study was supported by Deutsche Forschungsgemeinschaft (DFG) under grant DO 729/9. T. S. was also partly supported by the International Max Planck Research School for Elementary Processes in Physical Chemistry. The authors are grateful to Andre Fielicke, Cornelia Jäger, and Thomas Henning for fruitful discussions related to the properties of silicon clusters and interstellar silicate dust. We thank Julian Voß for support in the initial data acquisition of the EPD spectrum.

References

1 J. S. Mathis, *Annu. Rev. Astron. Astrophys.*, 1990, **28**(1), 37.
2 B. T. Draine, *Annu. Rev. Astron. Astrophys.*, 2003, **41**(1), 241.
3 F. Molster and C. Kemper, *Space Sci. Rev.*, 2005, **119**(1–4), 3.
4 T. Henning, *Annu. Rev. Astron. Astrophys.*, 2010, **48**(1), 21.
5 H.-P. Gail and E. Sedlmayr, *Physics and chemistry of circumstellar dust shells, Cambridge Astrophysics Series*, Cambridge University Press, New York, 2014, p. 52.
6 A. Sarangi, M. Matsuura and E. R. Micelotta, *Space Sci. Rev.*, 2018, **214**(3), 1.
7 D. Rogantini, E. Costantini, S. T. Zeegers, M. Mehdipour, I. Psaradaki, A. J. J. Raassen, C. P. de Vries and L. B. F. M. Waters, *Astron. Astrophys.*, 2020, **641**, A149.
8 S. T. Bromley, Silicate Nanoclusters: Understanding Their Cosmic Relevance from Bottom-Up Modelling, *Clusters*, Springer, Cham, 2017. pp. 237–68.
9 R. W. Wilson, A. A. Penzias, K. B. Jefferts, M. Kutner and P. Thaddeus, *Astrophys. J.*, 1971, **167**, L97.
10 D. F. Dickinson, *Astrophys. J.*, 1972, **175**, L43.
11 R. Mauersberger and C. Henkel, *Astron. Astrophys.*, 1991, **245**, 457.
12 B. A. McGuire, *Astrophys. J., Suppl. Ser.*, 2022, **259**(2), 30.
13 C. M. Lisse, C. H. Chen, M. C. Wyatt, A. Morlok, I. Song, G. Bryden and P. Sheehan, *Astrophys. J.*, 2009, **701**(2), 2019.
14 H. Fujiwara, T. Onaka, T. Yamashita, D. Ishihara, H. Kataza, M. Fukagawa, Y. Takeda and H. Murakami, *Astrophys. J. Lett.*, 2012, **749**(2), L29.
15 J. Crovisier, K. Leech, D. Bockelée-Morvan, T. Y. Brooke, M. S. Hanner, B. Altieri, H. U. Keller and E. Lellouch, *Science*, 1997, **275**(5308), 1904.
16 J. Dorschner, D. Fabian, T. Henning, C. Jäger and H. Mutschke, *Astron. Astrophys.*, 2000, **364**, 282.
17 K. Malfait, C. Waelkens, J. Bouwman, A. De Koter and L. Waters, *Astron. Astrophys.*, 1999, **345**, 181.
18 T. M. Steel and W. W. Duley, *Astrophys. J.*, 1987, **315**, 337.
19 A. C. Reber, S. Paranthaman, P. A. Clayborne, S. N. Khanna and A. W. Castleman, *ACS Nano*, 2008, **2**(8), 1729.
20 C. Koike, H. Chihara, A. Tsuchiyama, H. Suto, H. Sogawa and H. Okuda, *Astron. Astrophys.*, 2003, **399**(3), 1101.
21 A. Li and B. T. Draine, *Astrophys. J.*, 2002, **564**(2), 803.
22 S. Zhukovska, T. Henning and C. Dobbs, *Astrophys. J.*, 2018, **857**(2), 94.
23 M. C. McCarthy, C. A. Gottlieb and J. Cernicharo, *J. Mol. Spectrosc.*, 2019, **356**, 7.
24 H.-P. Gail and E. Sedlmayr, *Astron. Astrophys.*, 1999, **347**, 594.
25 A. G. G. M. Tielens, *Rev. Mod. Phys.*, 2013, **85**(3), 1021.
26 A. P. Ji, A. Frebel and V. Bromm, *Astrophys. J.*, 2014, **782**(2), 95.

27 G. Rouillé, C. Jäger and T. Henning, *Astrophys. J.*, 2020, **892**(2), 96.
28 S. A. Krasnokutski and F. Huisken, *J. Phys. Chem. A*, 2010, **114**(50), 13045.
29 S. A. Krasnokutski, G. Rouillé, C. Jäger, F. Huisken, S. Zhukovska and T. Henning, *Astrophys. J.*, 2014, **782**(1), 15.
30 R. Q. Zhang, M. W. Zhao and S. T. Lee, *Phys. Rev. Lett.*, 2004, **93**(9), 95503.
31 A. C. Reber, P. A. Clayborne, J. U. Reveles, S. N. Khanna, A. W. Castleman and A. Ali, *Nano Lett.*, 2006, **6**(6), 1190.
32 S. T. Bromley, J. C. Gómez Martín and J. M. C. Plane, *Phys. Chem. Chem. Phys.*, 2016, **18**(38), 26913.
33 T. P. M. Goumans and S. T. Bromley, *Mon. Not. R. Astron. Soc.*, 2012, **420**(4), 3344–3349.
34 S. Ramola, T. Belwal, C. J. Li, Y. X. Liu, Y. Y. Wang, S. M. Yang and C. H. Zhou, *J. Cleaner. Prod.*, 2021, **299**, 126802.
35 R. E. S. Clegg, L. J. van IJzendoorn and L. J. Allamandola, *Mon. Not. R. Astron. Soc.*, 1983, **203**(1), 125.
36 J. M. C. Plane, J. C. Gómez-Martín, W. Feng and D. Janches, *J. Geophys. Res.: Atmos.*, 2016, **121**(7), 3718.
37 W. D. Watson, *Rev. Mod. Phys.*, 1976, **48**(4), 513.
38 E. Herbst, *Annu. Rev. Phys. Chem.*, 1995, **46**(1), 27.
39 D. Gobrecht, I. Cherchneff, A. Sarangi, J. M. C. Plane and S. T. Bromley, *Astron. Astrophys.*, 2016, **585**, A6.
40 D. J. Fixsen and E. Dwek, *Astrophys. J.*, 2002, **578**(2), 1009.
41 W. R. Creasy, A. O'Keefe and J. R. McDonald, *J. Phys. Chem.*, 1987, **91**(11), 2848.
42 M. Jadraque, M. Santos, L. Díaz, J. Alvarez-Ruiz and M. Martín, *J. Phys. Chem. A*, 2009, **113**(41), 10880.
43 R. Torres and M. Martin, *Appl. Surf. Sci.*, 2002, **193**(1–4), 149.
44 N. K. Dzhemilev, S. F. Kovalenko, L. F. Lifanova, S. E. Maksimov and S. T. Khozhiev, *Bull. Russ. Acad. Sci.: Phys.*, 2008, **72**(7), 910.
45 S. K. Nayak, B. K. Rao, S. N. Khanna and P. Jena, *J. Chem. Phys.*, 1998, **109**(4), 1245.
46 K. Sen, D. Ghosh, S. Pakhira, T. Banu and A. K. Das, *J. Chem. Phys.*, 2013, **139**(23), 234303.
47 N. Goldberg, M. Iraqi, W. Koch and H. Schwarz, *Chem. Phys. Lett.*, 1994, **225**(4–6), 404.
48 M. Iraqi, N. Goldberg and H. Schwarz, *J. Phys. Chem.*, 1993, **97**, 11371.
49 J. C. Gómez Martín and J. M. C. Plane, *Phys. Chem. Chem. Phys.*, 2011, **13**(9), 3764.
50 X. Cheng, *Chem. Phys.*, 2021, **541**, 111047.
51 H.-B. Du, S.-P. Huang, A. de Sarkar, W.-J. Fan, Y. Jia and R.-Q. Zhang, *J. Phys. Chem. A*, 2014, **118**(39), 8893.
52 B. A. McGuire, O. Asvany, S. Brünken and S. Schlemmer, *Nat. Rev. Phys.*, 2020, **2**(8), 402.
53 B. R. Singh and P. Balk, *J. Electrochem. Soc.*, 1978, **125**(3), 453.
54 S. D. Rosner, R. Cameron, T. J. Scholl and R. A. Holt, *J. Mol. Spectrosc.*, 1998, **189**(1), 83.
55 P. R. Stollenwerk, B. C. Odom, D. L. Kokkin and T. Steimle, *J. Mol. Spectrosc.*, 2017, **332**, 26.
56 D. J. Lucas, L. A. Curtiss and J. A. Pople, *J. Chem. Phys.*, 1993, **99**(9), 6697.
57 D. P. Chong and Y. Takahata, *J. Electron Spectrosc. Relat. Phenom.*, 1977, **10**(2), 137.
58 D. Shi, W. Li, W. Xing, J. Sun, Z. Zhu and Y. Liu, *Comput. Theor. Chem.*, 2012, **980**, 73.
59 E. Garand, D. Goebbert, G. Santambrogio, E. Janssens, P. Lievens, G. Meijer, D. M. Neumark and K. R. Asmis, *Phys. Chem. Chem. Phys.*, 2008, **10**(11), 1502.
60 M. Savoca, J. Langer, D. J. Harding, D. Palagin, K. Reuter, O. Dopfer and A. Fielicke, *J. Phys. Chem.*, 2014, **141**(10), 104313.
61 R. R. Reddy, Y. Nazeer Ahammed, B. Sasikala Devi, K. Rama Gopal, P. Abdul Azeem and T. Rao, *Astrophys. Space Sci.*, 2002, **281**(4), 729.
62 M. Förstel, W. Schewe and O. Dopfer, *Angew. Chem.*, 2019, **131**(11), 3394.
63 M. Förstel, K. M. Pollow, K. Saroukh, E. A. Najib, R. Mitric and O. Dopfer, *Angew. Chem., Int. Ed.*, 2020, **59**(48), 21403.
64 M. Förstel, K. Pollow, T. Studemund and O. Dopfer, *Chem. – Eur. J.*, 2021, **27**(61), 15074.
65 M. Förstel, N.-N. Nahvi, K. Pollow, T. Studemund, A. E. Green, A. Fielicke, S. R. Mackenzie and O. Dopfer, *Nat. Sci.*, 2022, **3**, 1.
66 M. Förstel, R. G. Radloff, K. Pollow, T. Studemund and O. Dopfer, *J. Mol. Spectrosc.*, 2021, **377**, 111427.
67 T. Studemund, K. Pollow, S. Verhoeven, E. Mickein, O. Dopfer and M. Forstel, *J. Phys. Chem. Lett.*, 2022, **13**(33), 7624.
68 N. X. Truong, M. Savoca, D. J. Harding, A. Fielicke and O. Dopfer, *Phys. Chem. Chem. Phys.*, 2014, **16**(40), 22364.
69 M. Förstel, B. K. A. Jaeger, W. Schewe, P. H. A. Sporkhorst and O. Dopfer, *Rev. Sci. Instrum.*, 2017, **88**(12), 123110.
70 C. Walther, S. Becker, G. Dietrich, H.-J. Kluge, M. Lindinger, K. Lützenkirchen, L. Schweikhard and J. Ziegler, *Z. Phys. D: At., Mol. Clusters*, 1996, **38**(1), 51.
71 M. Schmidt, C. Ellert, W. Kronmüller and H. Haberland, *Phys. Rev. B: Condens. Matter Mater. Phys.*, 1999, **59**(16), 10970.
72 D. J. Wales and J. P. K. Doye, *J. Phys. Chem. A*, 1997, **101**(28), 5111.
73 A. D. Becke, *Phys. Rev. A: At., Mol., Opt. Phys.*, 1988, **38**(6), 3098.
74 F. Weigend, *Phys. Chem. Chem. Phys.*, 2006, **8**(9), 1057.
75 R. Ahlrichs, M. Bär, M. Häser, H. Horn and C. Kölmel, *Chem. Phys. Lett.*, 1989, **162**(3), 165.
76 M. Dupuis and J. B. Nicholas, *Mol. Phys.*, 1999, **96**(4), 549.
77 S. Grimme, J. Antony, S. Ehrlich and H. Krieg, *J. Chem. Phys.*, 2010, **132**(15), 154104.
78 S. Grimme, S. Ehrlich and L. Goerigk, *J. Comput. Chem.*, 2011, **32**(7), 1456.
79 M. J. Frisch, G. W. Trucks, H. B. Schlegel, G. E. Scuseria, M. A. Robb, J. R. Cheeseman, G. Scalmani, V. Barone, G. A. Petersson, H. Nakatsuji, X. Li, M. Caricato, A. V. Marenich, J. Bloino, B. G. Janesko, R. Gomperts, B. Mennucci, H. P. Hratchian, J. V. Ortiz, A. F. Izmaylov, J. L. Sonnenberg, D. Williams-Young, F. Ding, F. Lipparini, F. Egidi, J. Goings, B. Peng, A. Petrone, T. Henderson, D. Ranasinghe, V. G. Zakrzewski, J. Gao, N. Rega, G. Zheng, W. Liang, M. Hada, M. Ehara, K. Toyota, R. Fukuda, J. Hasegawa, M. Ishida, T. Nakajima, Y. Honda, O. Kitao, H. Nakai, T. Vreven, K. Throssell, J. A. Montgomery Jr., J. E. Peralta, F. Ogliaro, M. J. Bearpark, J. J. Heyd, E. N. Brothers,

K. N. Kudin, V. N. Staroverov, T. A. Keith, R. Kobayashi, J. Normand, K. Raghavachari, A. P. Rendell, J. C. Burant, S. S. Iyengar, J. Tomasi, M. Cossi, J. M. Millam, M. Klene, C. Adamo, R. Cammi, J. W. Ochterski, R. L. Martin, K. Morokuma, O. Farkas, J. B. Foresman and D. J. Fox, *Gaussian 16, Rev. C.01*, Wallingford, CT, 2016.

80 W. C. Lu, C. Z. Wang, V. Nguyen, M. W. Schmidt, M. S. Gordon and K. M. Ho, *J. Phys. Chem. A*, 2003, **107**(36), 6936.

81 L.-S. Wang, S. R. Desai, H. Wu and J. B. Nichloas, *Z. Phys. D*, 1997, **40**(1–4), 36.

82 N. X. Truong, M. Savoca, D. J. Harding, A. Fielicke and O. Dopfer, *Phys. Chem. Chem. Phys.*, 2015, **17**(29), 18961.

83 N. X. Truong, B. K. A. Jaeger, S. Gewinner, W. Schöllkopf, A. Fielicke and O. Dopfer, *J. Phys. Chem. C*, 2017, **121**(17), 9560.

84 D. L. Hildenbrand and E. Murad, *J. Chem. Phys.*, 1974, **61**(3), 1232.

85 W. C. Martin and R. Zalubas, *J. Phys. Chem. Ref. Data*, 1983, **12**(2), 323.

86 P. V. Avramov, I. Adamovic, K.-M. Ho, C. Z. Wang, W. C. Lu and M. S. Gordon, *J. Phys. Chem. A*, 2005, **109**(28), 6294.

87 L.-S. Wang, H. Wu, S. R. Desai, J. Fan and S. D. Colson, *J. Phys. Chem.*, 1996, **100**(21), 8697.

88 L.-S. Wang, J. B. Nicholas, M. Dupuis, H. Wu and S. D. Colson, *Phys. Rev. Lett.*, 1997, **78**(23), 4450.

